# Photocatalytic activation of sulfite by nitrogen vacancy modified graphitic carbon nitride for efficient degradation of carbamazepine

Jin Cao, Wenshan Nie, Long Huang, Yaobin Ding[*], Kangle Lv, Heqing Tang[*]

*Key Laboratory of Catalysis and Materials Science of the State Ethnic Affairs Commission and Ministry of Education, Hubei Province, College of Resources and Environmental Science, South-Central University for Nationalities, Wuhan 430074, PR China*

ABSTRACT

Graphitic carbon nitride with plentiful nitrogen vacancies (NV-g-$C_3N_4$) was prepared through a treatment of melamine under a $N_2$ flow, and used for constructing a system of sulfite activation under visible light toward the degradation of carbamazepine. In the presence of $Na_2SO_3$ (20 mmol $L^{-1}$), the use of NV-g-$C_3N_4$ (1 g $L^{-1}$) increased the apparent rate constant for the photodegradation of carbamazepine (42 µmol $L^{-1}$) to 0.0187 $min^{-1}$, with an increasing magnitude of 270% in comparison with that obtained by using the conventional g-$C_3N_4$ (Bulk-g-$C_3N_4$). The enhanced photodegradation of carbamazepine by NV-g-$C_3N_4$ was found to be attributed to the efficient trap of photo-generated electrons by nitrogen vacancies, which inhibited the recombination of photo-generated carriers. Therefore, more holes aggregating in the valence band were available for the activation of sulfite anions to produce sulfite radicals. Sulfite radicals were identified as the major reactive species in the investigated photocatalytic system for the degradation of carbamazepine. The degradation pathway of carbamazepine induced by sulfite radicals in the NV-g-$C_3N_4$/$Na_2SO_3$ system was clarified on the basis of the identification of intermediates by GC- and LC−MS. The photocatalytic activation of sulfite by metal free NV-g-$C_3N_4$ may be a useful technique for purifying waste-water containing organic pollutants.

## 1. Introduction

Pharmaceuticals and personal care products(PPCPs), as new emerging organic pollutants, have received increasing concern due to their high persistence to wastewater treatment and ubiquitous detection frequencies in various water systems [1]. As one of PPCPs, carbamazepine (CBZ) (5H-dibenzo [b, f] azepine-5-carboxamide) has been widely used in the treatment of epilepsy, psychomotor attacks and trigeminal neuralgia effects [2], and its annual consumption is about 1014 tons [3]. The wide use of CBZ results in a large number of the drug residue in the natural environment, which can finally affect water quality and drinking water supply, ecosystems and human health [4]. Since CBZ is a nitrogen-containing aromatic heterocyclic compound with a symmetrical structure, conventional biochemical treatment processes were found to be not effective for its removal [5,6]. Therefore, it is necessary to seek efficient technologies for the degradation of CBZ-containing waste-water.

To date, some physical and chemical techniques have been developed for CBZ removal, including adsorption [7], chlorination [8], electrochemical oxidation [9], ozonation [10], reverse osmosis [11] and advanced oxidation processes (AOPs) [12,13]. Among the AOPs,

sulfite radical ($SO_3^{\cdot-}$, $E° = 0.73$ V *vs* SHE) [14] has recently attracted attention as active species due to its high reactivity to degrade various organic substances [15], and low-cost generation from the activation of sulfite. Generally, sulfite radicals can be generated from the one-electron oxidation of sulfites or bisulfites [16], and the reported methods include photolysis of sulfite at moderate UV light [17,18], the activation of sulfite with transition metal ions ($Ce^{4+}$ [19], $Cr^{6+}$ [20], $Mn^{7+}$ [21]) and other radicals such as hydroxyl radicals [22]. It seems that the activation of sulfites is closely related to an oxidation step. Considering the oxidizing ability of photo-generated holes, it is expected that sulfite radicals can be generated from the oxidation of sulfite or bisulfite by photo-generated holes, and the effectiveness in the photocatalytic production of sulfite radicals is mainly dependent on the generation of photo-generated holes.

As a new type of metal free semiconductor material, graphitic carbon nitride (g-$C_3N_4$) was first introduced into the field of photocatalysis in 2009 [23]. It has a suitable band gap ($E_g = 2.7$ eV), and conduction band and valence band positions ($-1.3$ eV and $+1.4$ eV *vs* NHE), functioning as a good visible light driven photocatalyst [24]. However, bulk g-$C_3N_4$ usually shows low photocatalytic activity due to its high recombination of photo-generated carriers and low specific

surface area. To improve its photocatalytic activity, many strategies such as controlling shape [25], introducing heteroatoms (B, S, P, and Zn) [26,27], and coupling with dyes or other semiconductors [28] have been used to modify g-$C_3N_4$. Compared with the doping of foreign heteroatoms, the introduction of intrinsic vacancies in photocatalysts is a better selection due to the easy realization of these vacancies in the materials. It was reported that nitrogen vacancies (NVs) in g-$C_3N_4$ can trap photogenerated electrons to promote the separation of photogenerated carrier [29] and increase the amount of photogenerated holes. Therefore, we explored in the present work to develop a photocatalytic method of activating sulfite anions with g-$C_3N_4$ containing plentiful NVs for the production of sulfite radicals and degradation of organic contaminants.

Herein, NVs modified g-$C_3N_4$ (NV-g-$C_3N_4$) was prepared through a heat treatment of melamine under a $N_2$ flow, and thus used to the activate sulfite anions under visible light irradiation for promoting degradation of organic pollutants such as CBZ. Under the conditions of 1.0 g L$^{-1}$ NV-g-$C_3N_4$, 20 mmol L$^{-1}$ $Na_2SO_3$ and visible light irradiation, the removal of CBZ (42 μmol L$^{-1}$) was as high as 97% in 120 min, being much higher than that (56%) in the bulk-g-$C_3N_4$/$Na_2SO_3$ system. Based on the identification of intermediates by GC- and LC–MS, photocatalytic degradation pathways of CBZ were proposed.

## 2. Experimental section

### 2.1. Materials and chemicals

$Na_2SO_3$, HCl, NaOH, $Na_2SO_4$, $NaHCO_3$, $Na_2CO_3$, CBZ, melamine, ammonium oxalate (AO), methanol (MeOH), tertbutyl alcohol (TBA), isopropanol, naphthol and acetic acid ($C_2H_4O_2$) were provided by Sinopharm Chemical Reagent Co., Ltd. (Shanghai, China). 5,5-dimethyl-1-pyrroline-*N*-oxide (DMPO) and crocin were purchased from Aldrich. All the reagents were of analytical purity and were used as received. Ultrapure water (18.2 MΩ cm) was used for all the experiments.

### 2.2. Preparation of NV-g-$C_3N_4$ and bulk-g-$C_3N_4$

Bulk-g-$C_3N_4$ was synthesized by heating melamine according to a previous report [30]. Typically, melamine was placed in a covered crucible, and it was heated in a muffle furnace to 550 °C with a heating rate of 5 °C min$^{-1}$ and then hold for 3 h. NV-g-$C_3N_4$ was synthesized by heating melamine in a tube furnace at 550 °C with a heating rate of 5 °C min$^{-1}$ under a $N_2$ flow at 30 mL min$^{-1}$ and then hold for 3 h.

### 2.3. Characterization

Power X-ray diffraction (XRD) patterns were conducted on a Bruker D8 Advance X-ray diffractometer with Cu K$_a$ (λ = 1.5406 Å) radiation, operated at 40 mA and 40 kV. The morphology was investigated by scanning electron microscopy (SEM, ZEISS Sigma HD, Germany) with an acceleration voltage of 50 kV and transmission electron microscopy (TEM, FEI Tecnai TF20) with an acceleration voltage of 200 kV. Chemical compositions and the valence band (VB) were analyzed by X-ray photoelectron spectroscopy (XPS) on a ESCALAB 250XI spectrometer (Thermo Electron Corporation, USA). All the binding energies were calibrated to the C 1s peak at 284.6 eV of the surface adventitious carbon. The nitrogen-to-carbon (N/C) ratio of the samples was determined by X Ray fluorescence (XRF) (EDAX Inc, USA). Electron spin resonance (ESR) signals were recorded on a Bruker ESR EMX nano spectrometer at room temperature (298 K). The Brunauer-Emmett-Teller (BET) specific surface areas of the samples were determined by nitrogen adsorption at 77 K on an Autosorb-iQ (Quantachrome, USA) after vacuum degassing process at 300 ℃ overnight. UV–vis diffuse reflectance spectra (DRS) were obtained on a UV–vis spectrometer (Shimadzu UV-2600, Japan). Photoluminescence (PL) spectra were

recorded with a fluorescence spectrometer (F-7000, Hitachi, Japan) with excitation wavelength of 368 nm at room temperature. The electrochemical impedance spectroscopy (EIS) were performed on a CHI660 electrochemical workstation (Chenghua, Shanghai, China) by applying an AC voltage of 10 mV amplitude in the frequency range of $10^5$ Hz to $10^{-1}$ Hz with the initial potential (-0.3 V) in 0.5 M $Na_2SO_4$. For the photocurrent (PC) measurement, a 300 W xenon lamp with a 400-nm cutoff served as a light source and $Na_2SO_4$ (0.5 M) aqueous solution as the electrolyte. A standard three-electrode cell was used with the NV-g-$C_3N_4$ coated conductive glass electrode as a working electrode, a Pt electrode as auxiliary electrode, and a standard calomel electrode as reference electrode. The working electrodes was prepared as previously reported [31]. A fluorine doped tin oxide (FTO) glass plate with a size of 1.5 × 1 cm was sonicated in ethanol, and then rinsed with deionized water and dried in an air stream. A suspension of 75 mg of the powder in 1.5 mL of isopropanol and 20 μL naphthol were sonicated for 0.5 h, after that, the suspension was added dropwise to the FTO conductive glass. The coated glass was then dried under natural conditions.

### 2.4. Photocatalytic degradation experiments

The photocatalytic degradation of CBZ was conducted in the NV-g-$C_3N_4$/$Na_2SO_3$ system under visible-light (λ ≥ 400 nm) illumination. In a typical experiment, NV-g-$C_3N_4$ (1.0 g L$^{-1}$) was added into double deionized water containing 42 μmol L$^{-1}$ (10 mg L$^{-1}$) CBZ. After the suspension was stirred in dark for 30 min to reach the adsorption/desorption equilibrium, $Na_2SO_3$ (20 mmol L$^{-1}$) was added to the solution and the initial solution pH value was adjusted with 0.1 mmol L$^{-1}$ HCl and NaOH, the total volume of reaction solution was controlled at 50 mL. Then, a 500 W halogen tungsten lamp with a 400 nm cutoff was turned on, and the photocatalytic degradation of CBZ was started. An appropriate amount of the solution (about 1.5 mL) was sampled at given time intervals. The concentration of CBZ was measured by high performance liquid chromatography (HPLC). All measurements were repeated three times and the results were reproducible within experimental error ( ± 5%).

### 2.5. Chemical analysis

The concentration of residual CBZ in degradation solution was analyzed on a HPLC system (Agilent 1200 infinity series) with a G1315D 12600 DAD detector at a wavelength of 210 nm. An amethyst C18-P column (5 μm, 4.6 × 150 mm) was used as separation column and a mixture of methanol and water (50: 50, v/v) was used as the mobile phase with a flow rate of 1 mL min$^{-1}$. The injection volume was 20 μL.

To identify degradation intermediates, solution samples (2.0 mL) were taken after reaction time of 60 min in the NV-g-$C_3N_4$/$Na_2SO_3$ system. The degradation intermediates were detected by mass spectrometry on Bruker micrOTOF II LC/MS (USA) in electrospray positive ion (ESI$^+$) mode with methanol and water (50: 50, v/v) as the mobile phase with a flow rate of 1 mL min$^{-1}$ and an injection volume of 50 μL. Aromatic intermediates were also analyzed *via* GC–MS on a Thermo scientific TRACE 1300 GC Ultra system with the electron ionization mode. A TG-5MS capillary column (15 m × 0.25 mm × 0.25 μm) was used for analysis. Prior to GC–MS analysis, the supernatant (40 mL) was extracted with dichloromethane three times. The extract solution was dried over anhydrous $Na_2SO_4$ and concentrated to 1 mL by rotary evaporation. After the solvent was blown away, 1 mL trimethylchlorosilane and 0.2 mL bis(trimethylsilyl)trifluoroacetamide were added and it was kept at 50 °C for 30 min. The initial temperature of the column oven was maintained at 60 °C for 1 min and then increased to 280 °C with a heating rate of 6 °C min$^{-1}$. Helium was used as the carrier gas. Mass spectrometric detection was operated with 70 eV electron impact (EI) mode at an ionization current of 50 μA and an ion source
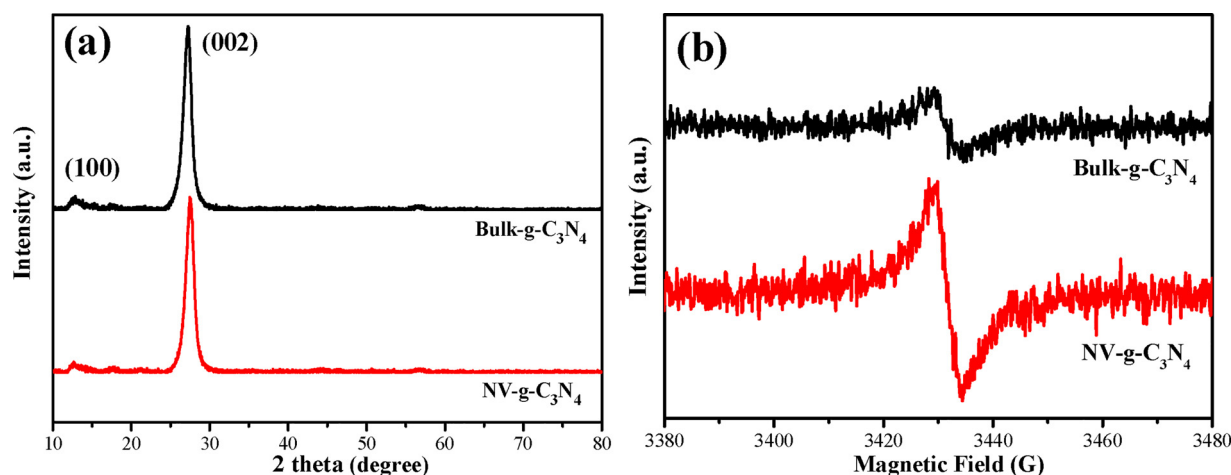
**Fig. 1.** (a) XRD patterns and (b) ESR spectra of bulk-g-$C_3N_4$ and NV-g-$C_3N_4$.

temperature of 250 °C. The mass spectra were recorded in full scan mode (*m/z* 50–1000) for qualitative analysis.

The concentrations of organic acids generated as intermediates were monitored on an ion chromatography system (TOSOH, IC-2010) equipped with TSK gel super IC-Anion HS (4.6 mm × 15 cm) analytical column, TSK guard column Super IC-A (4.6 mm × 10 cm), and a conductivity detector with a suppressor device. The mobile phase was 6.3 mmol $L^{-1}$ $NaHCO_3$ and 1.7 mmol $L^{-1}$ $Na_2CO_3$ at 0.8 mL $min^{-1}$, and the injection volume was 10 μL.

## 3. Result and discussion

### 3.1. Characterizations of NV-g-$C_3N_4$

Fig. 1a (and Fig. S1) showed the XRD patterns of bulk-g-$C_3N_4$ and NV-g-$C_3N_4$. Both samples have a strong peak of (002) at 2θ = 27.3° and a weak peak of (100) at about 12.7°. The (002) crystal plane with a strong diffraction peak was attributed to the layer stacking of aromatic systems. The (100) crystal plane was related to the in-planar repeating triazine unit. The (100) peak of the NV-g-$C_3N_4$ sample was slightly weaker than that of the bulk-g-$C_3N_4$ sample (Fig. S1a), signing a decrease in the order of filling of the in-plane structure. This result suggests that there may be many vacancies in the NV-g-$C_3N_4$ framework [32]. A careful comparison indicated that the diffraction peak of NV-g-$C_3N_4$ in the (002) crystal plane shifted toward a larger 2θ value of 27.6° (Fig. S1b), being indicative of a decrease in the repulsive force between the layers caused by the vacancies [33].

The existence of vacancies was further confirmed by solid ESR analysis. Generally, there are no ESR signal for a "perfect" g-$C_3N_4$ sample in the framework of which there are no nitrogen vacancies. If there are nitrogen vacancies in the framework of g-$C_3N_4$, a single Lorentzian line with a *g* value around 2 can be observed [32–35]. As shown in Fig. 1b, Lorentz lines from unpaired electrons on the aromatic ring carbon atoms were observed in both samples, suggesting nitrogen vacancies were formed in the as-prepared g-$C_3N_4$ samples [32,34]. The intensity of ESR signal gradually increases with the increase of the number of nitrogen vacancies in the framework of g-$C_3N_4$. The weak ESR signal intensity for bulk g-$C_3N_4$ suggested that there were a small number of **nitrogen vacancies in the framework of bulk g-$C_3$**$N_4$, and the much enhanced ESR signal indicated that NV-g-$C_3N_4$ had much more **nitrogen** vacancies [35].

The morphology of NV-g-$C_3N_4$ was observed by SEM and TEM (Fig. 2) in comparison with bulk-g-$C_3N_4$. As seen in Fig. 2 a and d, both NV-g-$C_3N_4$ and bulk-g-$C_3N_4$ displayed the typical morphologies of graphitic carbon nitride, which was composed of highly condense two-dimensional sheets. From the high magnification TEM images (Fig. 2e),

numerous mesopores with pore sizes ranging from 20 nm to 40 nm were apparently observed on the surface of NV-g-$C_3N_4$. In comparison, bulk-g-$C_3N_4$ tightly stacked by nanosheet and there were few visible hollow mesopores (Fig. 2b). Meanwhile, clear lattice fringes with an interplanar distance of 0.327 nm corresponding to the (002) plane of g-$C_3N_4$ was observed from the high resolution TEM image of bulk-g-$C_3N_4$ (Fig. 2c), and the interplanar distance in NV-g-$C_3N_4$ was decreased to 0.323 nm (Fig. 2f). This change was coincidence with the right shift of (002) peak in XRD pattern [36], which may be caused by the introduction of nitrogen vacancies. It was theoretically predicted that the layer stacking distance of layered g-$C_3N_4$ dominates the interlayer exciton dissociation and thus control the charge mobility. Reducing the stacking distance of π-π* layers between layers could improve lateral charge transport and interlayer exciton dissociation, and enhance photocatalytic activity [36].

The N/C atomic ratio of bulk-g-$C_3N_4$ and NV-g-$C_3N_4$ were evaluated by X-ray fluorescence spectroscopy (XRF). Based on the XRF analysis (Table S1), the atomic content of carbon and nitrogen was 38.9% and 57.9% for bulk-g-$C_3N_4$, and 40.9% and 56.5% for NV-g-$C_3N_4$. Accordingly, the N/C atomic ratio was calculated as 1.49 for bulk-g-$C_3N_4$ and 1.38 for NV-g-$C_3N_4$ (Fig. 3a). By the XPS analysis (Fig. S2 and Table S2), the surface atomic content of carbon and nitrogen was 43.7% and 52.0% for bulk-g-$C_3N_4$, and 46.6% and 48.4% for NV-g-$C_3N_4$, respectively. The surface N/C atomic ratio was calculated as 1.19 for bulk-g-$C_3N_4$ and 1.04 for NV-g-$C_3N_4$, being consistent with that reported by Yu et al. [37]. The increased N/C atomic ratios of NV-g-$C_3N_4$ from the XRF and XPS analysis suggest that more nitrogen vacancies have been generated in the NV-g-$C_3N_4$ framework.

Fig. 3b exhibited the high-resolution XPS spectrum of C 1 s, which could be fitted with three peaks with binding energies at 284.26, 285.55 and 287.42 eV, corresponding to $sp^2$ C−C bonds, C-$NH_X$ (x = 1, 2) species, and C−N−C coordination, respectively [32,34,38]. Compared with bulk-g-$C_3N_4$, a close observation showed that the intensity of the peak at 285.55 eV was weakened in NV-g-$C_3N_4$. Furthermore, the analysis of the XPS N 1 s spectra could also be fitted with three peaks (Fig. 3c). Based on previous reports [34,38], the peaks at 397.91, 398.69 and 400.25 eV were assigned to the $sp^2$-hybridized nitrogen (C−N−C), $sp^3$-tertiary nitrogen (N−$C_3$) and $NH_X$ groups, respectively (Table S2). Obviously, the C−N−C peak was much weakened in the case of NV-g-$C_3N_4$, and the atomic ratio of the N species in the form of C−N−C to that of N−$C_3$ was decreased from 4.2 for bulk-g-$C_3N_4$ to 3.8 for NV-g-$C_3N_4$. This clearly demonstrates that NVs mainly locate at the C−N−C lattice sites [39].

Fig. 3d presented FTIR spectra of bulk-g-$C_3N_4$ and NV-g-$C_3N_4$ samples, both of which exhibited typical IR patterns of graphitic carbon nitride, illustrating that the two samples have the basic atomic structure
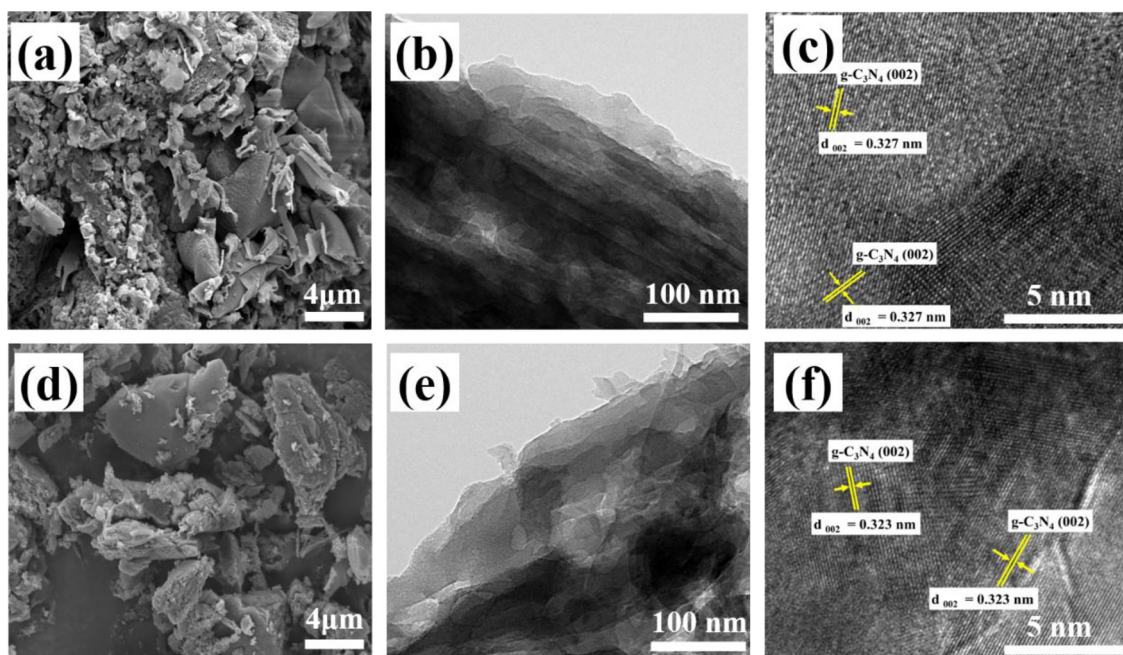
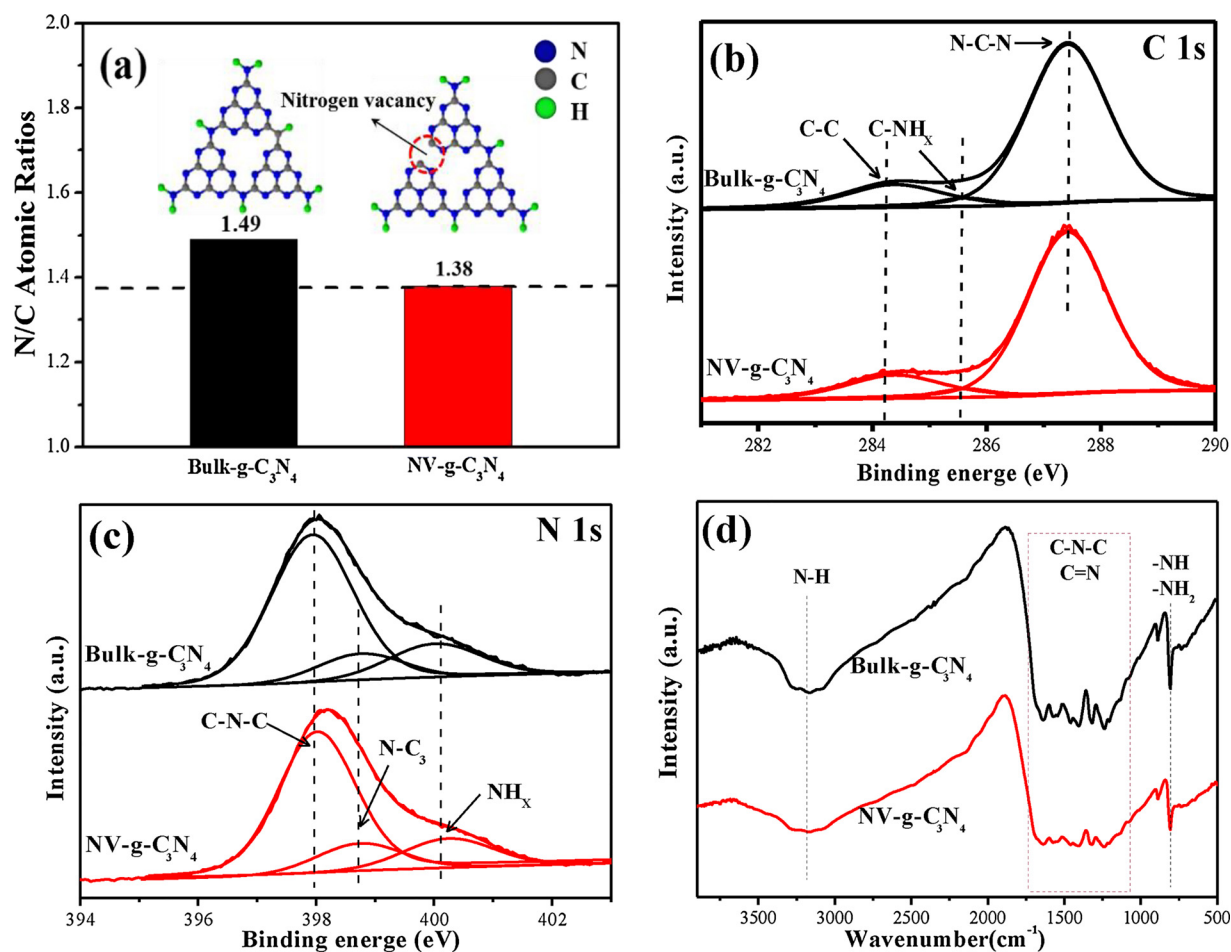**Fig. 2.** (a, d) SEM and (b, c, e, f) TEM images of (b, c) bulk-g-C$_3$N$_4$ and (e, f) NV-g-C$_3$N$_4$.



**Fig. 3.** Characterizations of bulk-g-C$_3$N$_4$ and NV-g-C$_3$N$_4$: (a) N/C atomic ratio, (b) C 1 s high-resolution XPS spectra, (c) N 1 s high-resolution XPS spectra, (d) FTIR spectra.
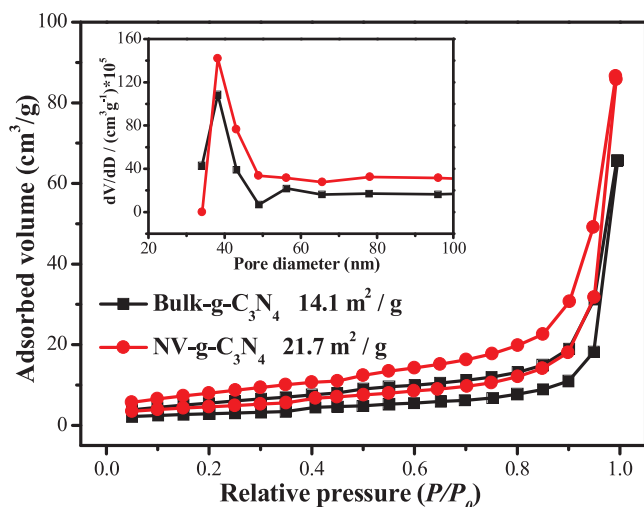
**Fig. 4.** $N_2$ sorption and desorption isotherms of bulk-g-$C_3N_4$ and NV-g-$C_3N_4$. The inset is the pore size distribution.

of g-$C_3N_4$. In details, a broad peak at around 3000-3500 cm$^{-1}$ revealed the existence of the O−H stretching vibrations of surface-absorption water molecules [39]. A sharp absorption at 810 cm$^{-1}$ was attributed the out-of-plane bending mode of heptazine rings, indicating the existence of the basic melon units with -NH/-NH$_2$ groups [38]. Additionally, several strong peaks in the region from 900 to 1800 cm$^{-1}$ were assigned to C−N−C and C=N heterocycles skeletal vibration of the aromatic ring [40]. The comparison between the two samples demonstrated that the intensities of the peak at around 810 cm$^{-1}$ and the peaks in the region from 900 to 1800 cm$^{-1}$ were correspondingly decreased in NV-g-$C_3N_4$, due to the existence of NVs in the framework of g-$C_3N_4$ [37–39]. This was consistent with the results of XRF and XPS analysis.

The textural properties of the samples were compared by the $N_2$ adsorption-desorption measurement (Fig. 4). The BET specific surface areas of bulk-g-$C_3N_4$ and NV-g-$C_3N_4$ were 14.1 and 21.7 m$^2$ g$^{-1}$, respectively. The Barret-Joyner-Halenda (BJH) analysis showed that NV-g-$C_3N_4$ possessed more abundant pores than bulk-g-$C_3N_4$ in the range from 34 to 48 nm, and they have the same pore diameter at 38.6 nm. These results illustrate that the introduction of NVs did not cause lattice collapse in the framework of g-$C_3N_4$, and but increased the internal specific surface area of NV-g-$C_3N_4$ [34,38].

### 3.2. Optical and photochemical properties

The optical properties of the bulk-g-$C_3N_4$ and NV-g-$C_3N_4$ samples were firstly investigated by DRS. It was found from Fig. 5a that the absorption edge of NV-g-$C_3N_4$ showed an obvious blue shift to 464 nm as compared to 480 nm for bulk-g-$C_3N_4$. As showed in Fig. 5b, the band gap ($E_g$) was calculated according to Tauc/David–Mott model described by the equation $(h\nu\alpha)^{1/n} = A(h\nu − E_g)$, where h is the Planck constant, $\nu$ is the frequency of vibration, $\alpha$ is the absorption coefficient, $E_g$ is the band gap, A is a proportional constant, and the value of the exponent n denotes the nature of the sample transition [41,42]. $E_g$ of NV-g-$C_3N_4$ was evaluated to be about 2.86 eV, being slightly larger than that of bulk-g-$C_3N_4$ (2.78 eV). The enlarged band gap of NV-g-$C_3N_4$ may be attributed to the quantum confinement effect (QCE) because of the introduction of NVs [32]. The band structures of the two samples were further examined by using valence band (VB) XPS analysis. As shown in Fig. 5c, the Fermi level ($E_F$) was located at 1.79 and 1.89 eV above the valence band maximum for bulk-g-$C_3N_4$ and NV-g-$C_3N_4$, respectively. Further, the band edge positions of the conduction band (CB) and valence band (VB) of bulk-g-$C_3N_4$ and NV-g-$C_3N_4$ can be calculated by using $E_{VB} = \triangle E - E_{vac} + W_s$ [42], where $\triangle E$ is the difference between

$E_F$ value and VB maximum value, $E_{vac}$ is the energy of free electrons in the hydrogen scale with a constant of 4.5 eV, and $W_s$ is work functions. The work function $W_s$ is 4.0 eV for g-$C_3N_4$ [43]. Hence, the VB positions of bulk-g-$C_3N_4$ and NV-g-$C_3N_4$ were determined as 1.29 and 1.39 eV, respectively. The more positive VB potential of NV-g-$C_3N_4$ than bulk-g-$C_3N_4$ indicated that NV-g-$C_3N_4$ had a strengthened oxidation potential, being important for the oxidation of sulfite to generate sulfite radicals. In addition, the CB edge potential ($E_{CB}$) was calculated by $E_{CB} = E_{VB} − E_g$ [44]. The VB position, CB position, and band gap $E_g$ for bulk-g-$C_3N_4$ and NV-g-$C_3N_4$ samples were obtained and summarized in Fig. 5d.

The recombination and separation of photo-generated electrons and holes in bulk-g-$C_3N_4$ and NV-g-$C_3N_4$ samples was studied by PL spectroscopy (Fig. 6). The emission peak at about 460 nm was attributed to the direct electron and hole recombination of band transition. Compared with bulk-g-$C_3N_4$, this emission in NV-g-$C_3N_4$ became weaker, demonstrating that the recombination of photo-generated electrons and holes in NV-g-$C_3N_4$ was greatly inhibited due to the introduction of NVs as an electron trapper.

To better illustrate the separation of photo-generated carriers, photoelectrochemical measurements were conducted. The photocurrent was carried out at a potential of 0.45 V, because the open circuit potential was measured as 0.45 V. At this potential, no current was generated in the blank solution. Therefore, we can reveal the real separation performance of photo-generated carrier at this potential. The photocurrent observed in Fig. 7a was anodic, suggesting that for both the photocatalysts NV-g-$C_3N_4$ and bulk-g-$C_3N_4$, photo-generated holes were the major carrier. As shown in Fig. 7a, the photocurrent density of the NV-g-$C_3N_4$ was about 1.6 times that of bulk-g-$C_3N_4$, meaning more photo-generated holes survived in NV-g-$C_3N_4$ photocatalytic system due to more efficient tapping of photo-generated electrons photo-generated electrons. Finally, there were more photo-generated holes involved in the activation of sulfite and induced the enhanced photodegradation of CBZ by NV-g-$C_3N_4$.

Additionally, electrochemical impedance spectroscopy (EIS) was performed to investigate charge migration and interfacial reaction capacity in photocatalytic materials, as showed in Fig. 7b. Obviously, the arc radius on the EIS plots of NV-g-$C_3N_4$ was much smaller than that of bulk-g-$C_3N_4$, implying that the introduction of NVs in g-$C_3N_4$ made photo-generated charge transfer easier.

### 3.3. Photocatalytic degradation of CBZ by NV-g-$C_3N_4$ and $Na_2SO_3$

Fig. 8a showed the kinetic data of the photocatalytic degradation of CBZ in different systems. The single use of either bulk-g-$C_3N_4$ or NV-g-$C_3N_4$ (1 g L$^{-1}$) in the absence of $Na_2SO_3$ brought about only 8% or 10% of CBZ removal in 120 min, respectively. The single use of $Na_2SO_3$ (20 mmol L$^{-1}$) under the illumination of visible light only induce 12% removal of CBZ. However, the simultaneous use of NV-g-$C_3N_4$ and $Na_2SO_3$ promoted the CBZ degradation significantly, yielding a CBZ removal of 97% in 120 min, which was much higher than that (56%) achieved by using bulk-g-$C_3N_4$ as the catalyst. The apparent pseudo-first-order rate constants were calculated by regression using a first-order decay model of -ln($c/c_0$) = $kt$, where $c_0$ is the initial concentration of CBZ, $c$ is the concentration after irradiation for a certain time $t$, and $k$ is the rate constant. As displayed in Fig. 8b, the rate constant for the degradation of CBZ in the system of NV-g-$C_3N_4$/$Na_2SO_3$ was 0.0187 min$^{-1}$, being about 2.7 times that in the system of bulk g-$C_3N_4$/$Na_2SO_3$ (0.0077 min$^{-1}$). The enhanced photocatalytic activity of NV-g-$C_3N_4$ for the activation of sulfite and degradation of CBZ was ascribed to the available of more photo-generated holes in the valence band, which can react with sulfite to produce more sulfite radicals. The mechanism was discussed in next section (section 3.5. Identification of main reactive species). TOC analysis was carried out to evaluate the mineralization extent of CBZ in the systems of bulk g-$C_3N_4$/$Na_2SO_3$ and NV-g-$C_3N_4$/$Na_2SO_3$ (Fig. S3). It was observed that after the photo-irradiation for 180 min, the use of NV-g-$C_3N_4$ yielded a TOC removal of
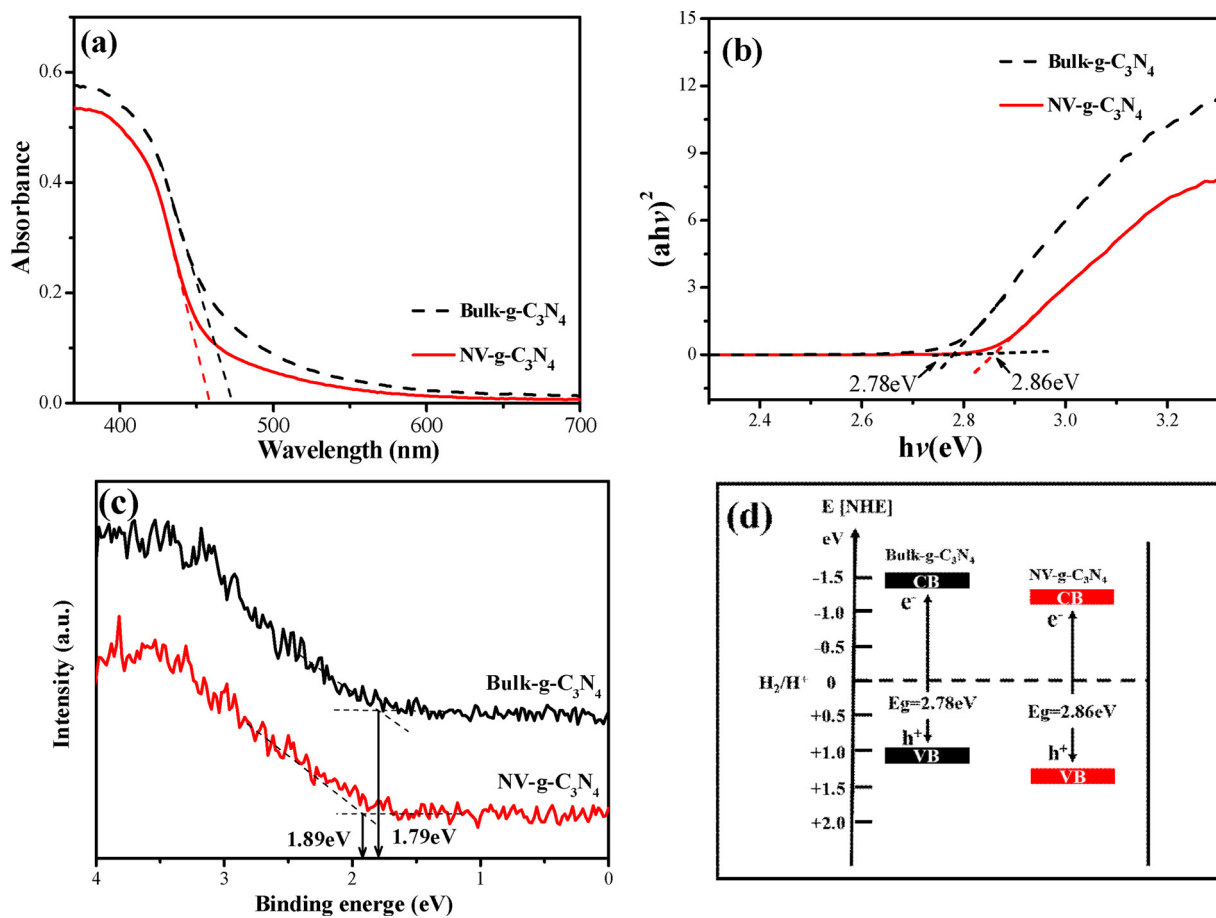
**Fig. 5.** (a) UV–vis diffuse reflectance spectra, (b) plots of $(ah\nu)^2$ *vs* photon energy, (c) VB XPS spectra, and (d) electronic band structures of bulk-g-$C_3N_4$ and NV–$C_3N_4$.
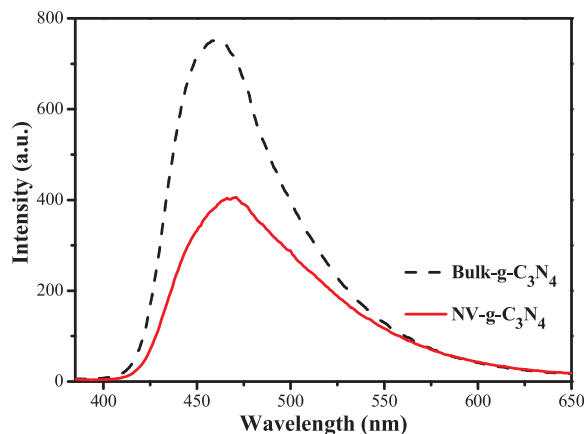


**Fig. 6.** Photoluminescence spectra of bulk-g-$C_3N_4$ and NV-g-$C_3N_4$.

25%, being considerably higher than that (10%) in the case of bulk g-$C_3N_4$.

NV-g-$C_3N_4$ was used as the photocatalyst to degrade other organic contaminants with diverse molecular structure including anionic dyes, cationic dyes, phenols, bisphenols and antibiotics in the presence of sulfite (Fig. S4). It was found that all the tested organic pollutants were readily degraded, illustrating the universality of the NV-g-$C_3N_4$/Na$_2$SO$_3$ system in the treatment of organic pollutants with different chemical structures. To check the stability of NV-g-$C_3N_4$ and bulk-g-$C_3N_4$ as photocatalysts, we carried out the CBZ degradation by recycling and reusing them for five successive cycles. After the degradation was

finished for the first cycle, the used catalyst was collected by vacuum filtration, washed with water several times, and re-dispersed in the fresh CBZ solution. Then, 20 mmol L$^{-1}$ Na$_2$SO$_3$ was added, and the second cycle of degradation was conducted. These steps were repeated several times. As shown in Fig. S5a, the CBZ removal by NV-g-$C_3N_4$ was still about 90% after the fifth run, indicating the excellent stability of NV-g-$C_3N_4$ catalyst. The degradation of CBZ by bulk-g-$C_3N_4$ also did not changed markedly after five cycles. In addition, the 5-run experiments did not induce obvious change of XRD characteristic peaks of NV-g-$C_3N_4$ and bulk-g-$C_3N_4$ (Fig. S5b and Fig. S5c), suggesting that both two catalysts were stable under ambient conditions.

The effect of Na$_2$SO$_3$ concentration in the range of 5–50 mmol L$^{-1}$ on the catalytic activity of NV-g-$C_3N_4$ (1 g L$^{-1}$) was investigated in the presence of 20 mg L$^{-1}$ CBZ. As displayed in Fig. 8a and Fig. S6a, only 10% of CBZ removal was obtained in 120 min without the addition of sulfite. The removal of CBZ was promoted to 82% and 97% when the concentration of sulfite was 10 and 20 mmol L$^{-1}$, respectively, corresponding to an increase of the rate constant for the degradation of CBZ by 16.9 and 26.1 times (Fig. 9a). When the concentration of sulfite was further increased, the increase of the rate constant for the degradation of CBZ was less significant.

Fig. 9b and Fig. S6b illustrated the influence of initial solution pH on the rate constant of the degradation of CBZ in the NV-g-$C_3N_4$/Na$_2$SO$_3$ system. It was observed that the degradation rate constant was increased slowly with increasing pH$_0$ up to pH 7, but drastically declined at higher pH$_0$ values. This was mainly attributed to the surface potential of NV-g-$C_3N_4$ and the distribution of sulfite under different pH conditions. As seen in Fig. S7, NV-g-$C_3N_4$ had a point of zero charge (pH$_{pzc}$) at a pH of around 6.3. The surface charge of NV-g-$C_3N_4$ was
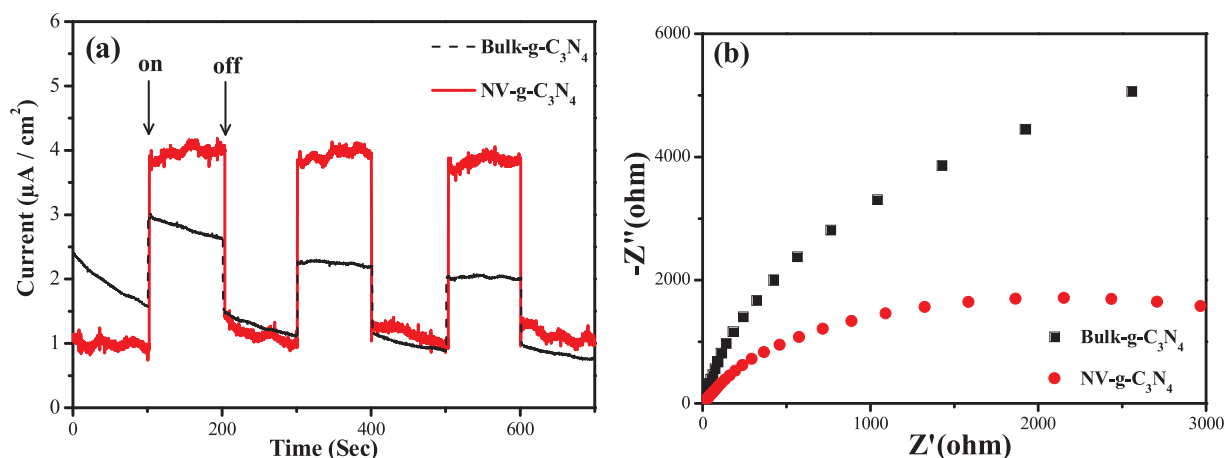
**Fig. 7.** (a) Transient photocurrent responses and (b) electrochemical impedance spectra of bulk-g-C$_3$N$_4$ and NV-g-C$_3$N$_4$.

positive at pH < 6.3 and negative when pH > 6.3. On the other hand, sulfite mainly exists as H$_2$SO$_3$ when pH < 2, and HSO$_3^-$ occupied 90% within the pH range of 2.8–6.3, however, SO$_3^{2-}$ become dominant as the pH value is increased under alkaline conditions (Fig. S8). Therefore, in the neutral pH solution, the positively charged surface of NV-g-C$_3$N$_4$ is favorable to the adsorption of HSO$_3^-$ due to electrostatic attraction, which prompts the in-situ activation of adsorbed sulfite by photo-generated holes on the surface of NV-g-C$_3$N$_4$. The high efficiency of the photocatalytic activation of sulfite by NV-g-C$_3$N$_4$ at a neutral pH highlights its advantage and promise for the treatment of practical wastewater with pH generally in the range of 6–8. A similar trend was also observed in the bulk-g-C$_3$N$_4$/Na$_2$SO$_3$ system (Fig. S9). A major difference was that the highest rate constant for the degradation of CBZ by bulk-g-C$_3$N$_4$ was obtained as 0.0094 min$^{-1}$ at pH$_0$ 5. However, this rate constant value was much lower than that (0.018 min$^{-1}$) observed for NV-g-C$_3$N$_4$ at the same pH$_0$. These results suggested the important role of nitrogen vacancies for the efficient separation of photo-generated carriers in NV-g-C$_3$N$_4$.

### 3.4. Identification of main reactive species

To identify the active species in the photocatalytic degradation process, several types of scavengers were added into the NV-g-C$_3$N$_4$/Na$_2$SO$_3$ system under visible light illumination. Because the reaction between TBA and ·OH is rapid ($6.0 \times 10^8$ M$^{-1}$ s$^{-1}$) [45], TBA was used as a quencher for ·OH. As illustrated in Fig. 10a, the addition of TBA had no significant effect on CBZ degradation, indicating that the

generation of ·OH was very minor, if any, in the NV-g-C$_3$N$_4$/Na$_2$SO$_3$ system. MeOH was added into the reaction solution to check whether there were other free radicals being involved in the degradation of CBZ. As shown in Fig. 10a, the addition of MeOH nearly completely inhibited the degradation of CBZ, which attest that free radicals were generated from the photocatalytic activation of sulfite, being mainly responsible for the degradation of CBZ. Moreover, when AO was used as a quencher for holes (h$^+$) [46], the removal of CBZ was also hampered greatly. These results indicate that both holes and SO$_3^{·-}$ play vital roles in the degradation of CBZ. However, as shown in Fig. 8a, CBZ could be hardly degraded in the NV-g-C$_3$N$_4$ photocatalytic system, suggesting that photo-generated holes alone were inefficient for the degradation of CBZ. Therefore, based on the results above, it was concluded that SO$_3^{·-}$ was the main reactive species for the degradation of CBZ in the NV-g-C$_3$N$_4$/Na$_2$SO$_3$ system.

In order to gain direct evidence for the involvement and the formation process of reactive species, electron spin resonance (ESR) analysis was employed using DMPO as trapping agent. As shown in Fig. 10b, the significant signals of DMPO-SO$_3^{·-}$ adducts were observed in the NV-g-C$_3$N$_4$/Na$_2$SO$_3$ system. In comparison, there is no obvious ESR signal of DMPO-SO$_3^{·-}$ when AO was added to quench photo-generated holes in the NV-g-C$_3$N$_4$/Na$_2$SO$_3$ system. The result indicates that SO$_3^{·-}$ was generated from the oxidation of sulfite anions by photo-generated holes according to the following equation.

$$h^+ + SO_3^{2-} \rightarrow SO_3^{·-} \tag{1}$$

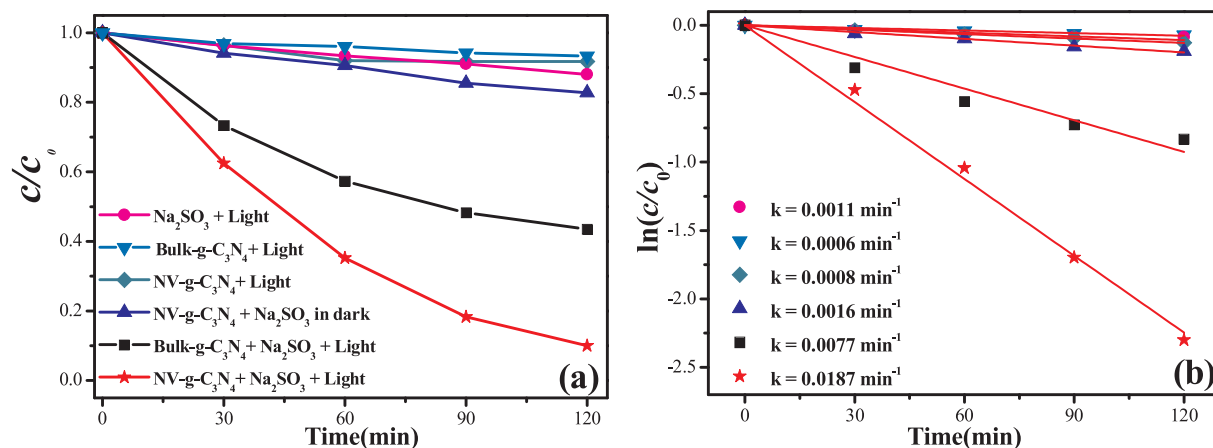In the presence of excess sulfite anions, photo-generated holes could



**Fig. 8.** (a) Degradation kinetics of CBZ and (b) kinetic fitting of the CBZ degradation in different systems. Reaction conditions: initial CBZ concentration 42 μmol L$^{-1}$, initial Na$_2$SO$_3$ concentration 20 mmol L$^{-1}$, initial pH = 7, and catalyst load 1 g L$^{-1}$.
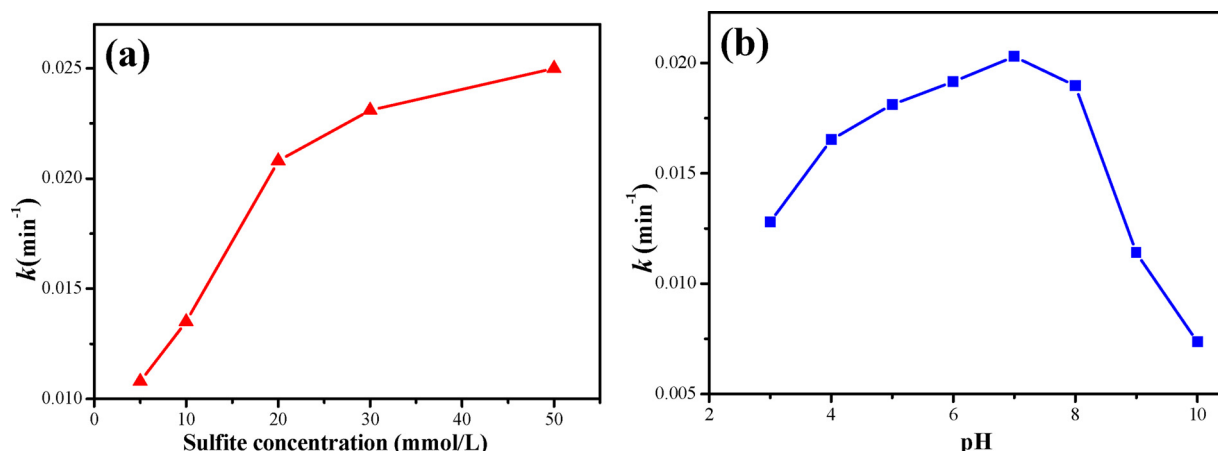
**Fig. 9.** Effects of (a) $Na_2SO_3$ concentration and (b) initial solution pH on the apparent pseudo-first-order rate constant ($k$) of CBZ degradation.

all transform to $SO_3^{\cdot-}$ according to the Eq. (1). Moreover, as seen in Fig. 10b, the intensity for the signal of DMPO-$SO_3^{\cdot-}$ in the NV-g-$C_3N_4$/$Na_2SO_3$ system was much stronger than that in the bulk-g-$C_3N_4$/$Na_2SO_3$ system, which is consistent with the higher CBZ degradation in the NV-g-$C_3N_4$/$Na_2SO_3$ system. This might be caused by the high separation of photo-generated holes-electrons in the NV-g-$C_3N_4$ as proved by photo-luminescence (PL) spectroscopy (Fig. 6) and transient photocurrent response (Fig. 7).

After $SO_3^{\cdot-}$ was identified as the major reactive species for the photocatalytic degradation of CBZ, the residual of $SO_3^{\cdot-}$ in NV-g-$C_3N_4$/$Na_2SO_3$ and bulk-g-$C_3N_4$/$Na_2SO_3$ system were measured. As previously reported [15], $SO_3^{\cdot-}$ has a relatively higher first-order rate constant with crocin ($r = 1.0 \times 10^9$ L mol$^{-1}$ s$^{-1}$), crocin was used as a probe to measure the amount of $SO_3^{\cdot-}$. As seen in Fig. S10, the rate constant ($k$) of the reaction of sulfite radicals with crocin in the NV-g-$C_3N_4$/$Na_2SO_3$ and bulk-g-$C_3N_4$/$Na_2SO_3$ systems were 0.0244 s$^{-1}$ and 0.0078 s$^{-1}$, respectively. According to the first-order reaction rate equation $r = -dc/dt = kc$, where $c$ is the concentration of sulfite radicals, the concentration of $SO_3^{\cdot-}$ in the systems of NV-g-$C_3N_4$/$Na_2SO_3$ and bulk-g-$C_3N_4$/$Na_2SO_3$ system was calculated as $2.4 \times 10^{-11}$ and $7.8 \times 10^{-12}$ mol L$^{-1}$. This further confirms that NV-g-$C_3N_4$ is better for the photo-catalytic activation of sulfite.

Generally, the trapped electrons will react with oxygen or $H_2O$ in aqueous solution, dependent on the dissolved oxygen concentration in aqueous solution. In the present work, the addition of sulfite consumed greatly the dissolved oxygen (Fig. S11), and the activation of oxygen by

photo-generated electrons was greatly depressed. This was proved by ESR results. We used ESR to detect the formation of $O_2^{\cdot-}$. However, no signal of $O_2^{\cdot-}$ was detected in the visible light irradiated sulfite/NV-g-$C_3N_4$ system (Fig. S12). Therefore, we inferred that the trapped electrons reacted with $H_2O$, leading to the generation of $H_2$ in the studied system. We further checked the formation of $H_2$ during the CBZ degradation in visible light irradiated sulfite/NV-g-$C_3N_4$ system. As shown in Fig. S13, 27.6 μmol $H_2$ was generated under the conditions of 20 mmol L$^{-1}$ sulfite, 1.0 g L$^{-1}$ NV-g-$C_3N_4$ and 42 μmol L$^{-1}$ CBZ. Therefore, it can be concluded that **the photo-generated electrons were firstly trapped by nitrogen vacancies on the surface of NV-g-$C_3N_4$, and then reduced $H_2O$ to generate $H_2$ [47].**

### 3.5. Degradation pathway of CBZ induced by sulfite radicals

Seven intermediates were detected and tentatively identified as the intermediates of CBZ degradation in the NV-g-$C_3N_4$/$Na_2SO_3$ system by LC−MS (Table S4). As represented in Fig. S14, the MS spectrum showed $[M+H]^+$ molecular ion peak at $m/z$ 237.1 with the retention time of 14.7 min, which was attributed to the parent compound of CBZ with the formula of $C_{15}H_{12}N_2O$ (M = 236). The intermediate at $m/z = 253.1$ (P4) was identified as 10,11–10,11-epoxycarbamazepine, which is one of the most frequently detected intermediates from the oxidation of CBZ [6]. P4 was proposed to be generated from the direct attack of the olefinic double bond on the central azepine ring of CBZ by $SO_3^{\cdot-}$. Concretely, the intermediate P4 was transformed to acridinium-9-
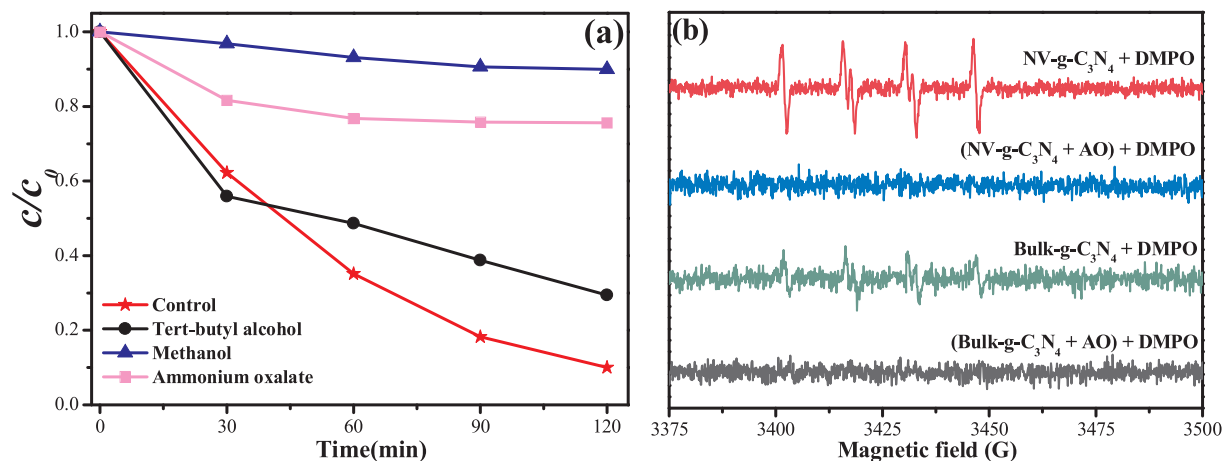


**Fig. 10.** (a) Effect of scavengers on photocatalytic degradation of CBZ in NV-g-$C_3N_4$/$Na_2SO_3$ system and (b) ESR spectra trapped by DMPO after 10 min of UV-light irradiation in the NV-g-$C_3N_4$/$Na_2SO_3$ system. Reaction conditions: scavenger concentration 50 mmol L$^{-1}$, $Na_2SO_3$ concentration 20 mmol L$^{-1}$, DMPO concentration 25 mmol L$^{-1}$, and pH 7.0.
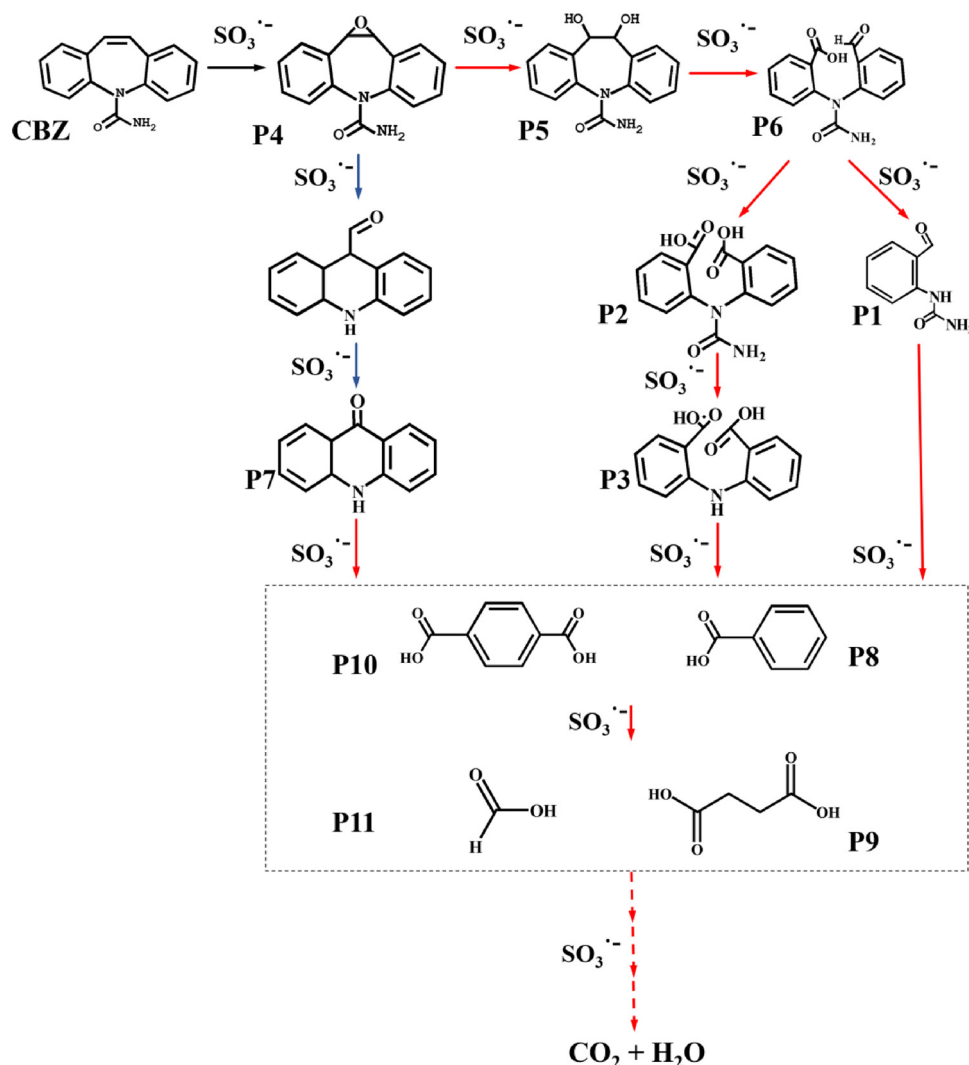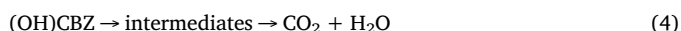
**Fig. 11.** Proposed oxidative degradation pathways of CBZ by $SO_3^{\cdot-}$ in the NV-g-C$_3$N$_4$/Na$_2$SO$_3$ system.

carbaldehyde by a facile ring contraction [12], and then further transformed to P7 *via* the cleavage of an aldehyde group under the action of $SO_3^{\cdot-}$. Similar intermediates were usually observed in the photoinduced degradation systems such as UV-radiation [48], UV/ H$_2$O$_2$ [12] and BiPO$_4$ based photocatalytic systems [49]. Moreover, the intermediate P5 at *m/z* 271.1 and a fragment at *m/z* 272 corresponding to the consecutive loss of H group was identified as 10,11-dihydro-di-hydroxycarbamazepine ((OH)CBZ). Similar degradation intermediates have been reported during the oxidation of CBZ by hydroxyl and sulfate radicals [49–51]. A possible mechanism is electrophilic attack at the olefinic double bond on the central heterocyclic ring of CBZ *via* hydroxyl or sulfate radicals [49–52]. The detection of the dihydroxylated intermediate (P5) suggests that the attack of organic pollutants such as CBZ by $SO_3^{\cdot-}$ was an electron transfer reaction, which can be explained by the following reactions (Eqs. (2)–(4)):

$$CBZ + SO_3^{\cdot-} \rightarrow CBZ^{\cdot+} + SO_3^{2-} \tag{2}$$

$$CBZ^{\cdot+} + H_2O \rightarrow (OH)CBZ + H^+ \tag{3}$$

$$(OH)CBZ \rightarrow intermediates \rightarrow CO_2 + H_2O \tag{4}$$

In the same way, the intermediates P6 and P2 were formed from the oxidative attack of P5 by $SO_3^{\cdot-}$. In addition to the attack of $SO_3^{\cdot-}$ on the middle carbon atom, the hydrolysis of the urea group on the central heterocyclic ring of CBZ was also involved in the degradation of CBZ [53]. In this way, intermediate P3 was generated. Besides, P1 at *m/z*

164.9 was identified as (2-formyl-phenyl)-urea, which has not been reported as an intermediate of CBZ degradation on the literature. The proposed mechanism is the attack of urea group on the central heterocyclic ring of the intermediate P6 by $SO_3^{\cdot-}$.

Moreover, other three intermediates (P8, P9 and P10) were identified by GC−MS as benzoic acid, succinic acid and terephthalic acid (Fig. S15). They might be formed from P1, P3 and P7 *via* attacking by $SO_3^{\cdot-}$ on urea or imine groups. And P9 was detected as a ring-rupturing reaction product. By using IC analysis (Fig. S16), formic acid (P11) was identified as another CBZ ring opening product from the further oxidation of intermediates. Based on the above results and the literatures on the oxidative degradation of CBZ [51–55], the oxidative degradation pathway of CBZ by $SO_3^{\cdot-}$ in the NV-g-C$_3$N$_4$/Na$_2$SO$_3$ system was proposed in Fig. 11.

## 4. Conclusions

A new photocatalytic system for the activation of sulfite was developed by using metal free and nitrogen vacancy modified graphitic carbon nitride (NV-g-C$_3$N$_4$) as a visible light photocatalyst. This photocatalytic system was confirmed to be efficient for the degradation of carbamazepine (CBZ). It was found that the introduction of NVs in g-C$_3$N$_4$ obviously enhanced the activation ability of sulfite to sulfite radicals, and thus the degradation of CBZ. Under conditions of 1.0 g L$^{-1}$ NV-g-C$_3$N$_4$, 20 mmol L$^{-1}$ Na$_2$SO$_3$ and 10 ppm CBZ, a CBZ removal of

97% was achieved in 120 min under visible light illumination, being much higher than that (56%) in the bulk-g-$C_3N_4$/$Na_2SO_3$ system. Through characterizations by photoluminescence spectroscopy and transient photocurrent response, it was observed that the introduced NVs could efficiently trap photo-generated electrons, thus inhibiting the recombination of photo-generated carriers and surviving more holes for the activation of sulfite anions to produce $SO_3^{\cdot-}$. In the newly developed $SO_3^{\cdot-}$ systems, eleven degradation intermediates were identified by GC−MS, LC−MS and IC. The proposed degradation mechanism of CBZ by $SO_3^{\cdot-}$ was divided into two modes: the attack of the olefinic double bond on the central heterocyclic ring and the hydrolysis of urea groups on the central heterocyclic ring of CBZ.

## Acknowledgements

## Appendix A. Supplementary data

Supplementary material related to this article can be found, in the online version, at doi:https://doi.org/10.1016/j.apcatb.2018.09.007.

## References

[1] B.H. Sørensen, S.N. Nielsen, P.F. Lanzky, F. Ingerslev, H.C. Holten Lützhøft, S.E. Jørgensen, Chemosphere 36 (1998) 357–393.
[2] M.A. Rogawski, Epilepsy Res. 68 (2006) 22–28.
[3] Y. Zhang, S.U. Geissen, C. Gal, Chemosphere 73 (2008) 1151–1161.
[4] T. Heberer, Toxicol. Lett. 131 (2002) 5–17.
[5] C. Martínez, M. Canle, L.M.I. Fernández, J.A. Santaballa, J. Faria, Appl. Catal. B: Environ. 102 (2011) 563–571.
[6] T.E. Doll, F.H. Frimmel, Catal. Today 101 (2005) 195–202.
[7] N. Suriyanon, P. Punyapalakul, C. Ngamcharussrivichai, Chem. Eng. J. 214 (2013) 208–218.
[8] M. Soufan, M. Deborde, A. Delmont, B. Legube, Water Res. 47 (2013) 5076–5087.
[9] A.M. Urtiaga, G. Pérez, R. Ibáñez, I. Ortiz, Desalination 331 (2013) 26–34.
[10] D.C. McDowell, M.M. Huber, M. Wagner, U. von Gunten, T.A. Ternes, Environ. Sci. Technol. 39 (2005) 8014–8022.
[11] P. Westerhoff, H. Moon, D. Minakata, J. Crittenden, Water Res. 43 (2009) 3992–3998.
[12] D. Vogna, R. Marotta, R. Andreozzi, A. Napolitano, M. d'Ischia, Chemosphere 54 (2004) 497–505.
[13] J. Deng, Y. Shao, N. Gao, S. Xia, C. Tan, S. Zhou, X. Hu, Chem. Eng. J. 222 (2013) 150–158.
[14] T.N. Das, R.E. Huie, P. Neta, J. Phys. Chem. A 103 (1999) 3581–3588.
[15] M.E. Russ, C. Michel, W. Bors, M. Saran, Radiat. Environ. Bioph. 26 (1987) 289–294.
[16] J. Zhang, L. Zhu, Z. Shi, Y. Gao, Chemosphere 186 (2017) 576–579.
[17] B.P. Vellanki, B. Batchelor, A. Abdel-Wahab, Environ. Eng. Sci. 30 (2013) 264–271.
[18] X. Liu, B.P. Vellanki, B. Batchelor, A.A. Wahab, Chem. Eng. J. 237 (2014) 300–307.
[19] T. Ozawa, T. Kwan, Chem. Commun. (1983) 80–81.
[20] B. Jiang, Y. Liu, J. Zheng, M. Tan, Z. Wang, M. Wu, Environ. Sci. Technol. 49 (2015) 12363–12371.
[21] J. Jiang, S.Y. Pang, J. Ma, H. Liu, Environ. Sci. Technol. 46 (2012) 1774–1781.
[22] W. Deng, H. Zhao, F. Pan, X. Feng, B. Jung, A.A. Wahab, B. Batchelor, Y. Li, Environ. Sci. Technol. 51 (2017) 13372–13379.
[23] S.C. Yan, Z.S. Li, Z.G. Zou, Langmuir 25 (2009) 10397–10401.
[24] S.C. Yan, Z.S. Li, Z.G. Zou, Langmuir 26 (2010) 3894–3901.
[25] X. Wang, K. Maeda, X. Chen, K. Takanabe, Y. Domen, Y. Hou, X. Fu, J. Am. Chem. Soc. 131 (2009) 1680–1681.
[26] G. Liu, P. Niu, C. Sun, S.C. Smith, Z. Chen, G.Q. Lu, H.-M. Cheng, J. Am. Chem. Soc. 132 (2010) 11642–11648.
[27] S. Yan, Z. Li, Z. Zou, Langmuir 26 (2010) 3894–3901.
[28] Y. Wang, R. Shi, J. Lin, Y. Zhu, Energy Environ. Sci. 4 (2011) 2922–2929.
[29] Q. Tay, P. Kanhere, C.F. Ng, S. Chen, S. Chakraborty, A.C.H. Huan, T.C. Sum, R. Ahuja, Z. Chen, Chem. Mater. 27 (2015) 4930–4933.
[30] X. Wang, K. Maeda, A. Thomas, K. Takanabe, G. Xin, J.M. Carlsson, K. Domen, M. Antonietti, Nat. Mater. 8 (2008) 76–80.
[31] T. Kawahara, K. Yamada, H. Tada, J. Colloid, Interf. Sci. 294 (2006) 504–507.
[32] G. Dong, W. Ho, C. Wang, J. Mater. Chem. A 3 (2015) 23435–23441.
[33] P. Niu, G. Liu, H.M. Cheng, J. Phys. Chem. C 116 (2012) 11013–11018.
[34] Z. Hong, B. Shen, Y. Chen, B. Lin, B. Gao, J. Mater. Chem. A 1 (2013) 11754–11761.
[35] J. Zhang, M. Zhang, R. Sun, Z. Wang, Angew. Chem. Int. Edit. 124 (2012) 10292–10296.
[36] J.S. Cheng, Z. Hu, K.L. Lv, X.F. Wu, Q. Li, Y.H. Li, X.F. Li, J. Sun, Appl. Catal. B: Environ. 232 (2018) 330–339.
[37] H. Yu, R. Shi, Y. Zhao, T. Bian, Y. Zhao, C. Zhou, G.I.N. Waterhouse, L. Wu, C. Tung, T. Zhang, Adv. Mater. 29 (2017) 1605148.
[38] J. Ding, W. Xu, H. Wan, D. Yuan, C. Chen, L. Wang, G. Guan, W. Dai, Appl. Catal. B: Environ. 221 (2018) 626–634.
[39] P. Niu, L.C. Yin, Y.Q. Yang, G. Liu, H.M. Cheng, Adv. Mater. 26 (2014) 8046–8052.
[40] P. Niu, M. Qiao, Y. Li, L. Huang, T. Zhai, Nano Energy 44 (2018) 73–81.
[41] Y. Zang, L. Li, X. Xiao, R. Lin, G. Li, Chem. Eng. J. 246 (2014) 277–286.
[42] Y. Qin, Y. Ding, H. Tang, J. Environ. Chem. Eng. 4 (2016) 4374–4384.
[43] W. Chen, Z. Chen, T. Liu, Z. Jia, X. Liu, J. Environ. Chem. Eng. 2 (2014) 1889–1897.
[44] H. Shi, G. Chen, C. Zhang, Z. Zou, ACS Catal. 4 (2014) 3637–3643.
[45] P. Neta, R.E. Huie, A.B. Ross, J. Phys. Chem. Ref. Data 17 (1988) 1027–1284.
[46] Y. Zhang, N. Zhang, Z.-R. Tang, Y.-J. Xu, Chem. Sci. 4 (2013) 1820–1824.
[47] Y. Mao, Y. Wu, G. Li, P. Dai, X. Yu, Z. Bai, P. Chen, Reac. Kinet. Mech. Cat. (2018) 1–12.
[48] T. Kosjek, H.R. Andersen, B. Kompare, A. Ledin, E. Heath, Environ. Sci. Technol. 43 (2009) 6256–6261.
[49] J. Xu, L. Li, C. Guo, Y. Zhang, W. Meng, Appl. Catal. B: Environ. 130–131 (2013) 285–292.
[50] M.M. Ahmed, S. Chiron, Water Res. 48 (2014) 229–236.
[51] Y.F. Rao, L. Qu, H. Yang, W. Chu, J. Hazard. Mater. 268 (2014) 23–32.
[52] A. Ghauch, H. Baydoun, P. Dermesropian, Chem. Eng. J. 172 (2011) 18–27.
[53] Y. Ding, G. Zhang, X. Wang, L. Zhu, H. Tang, Appl. Catal. B: Environ. 202 (2017) 528–538.
[54] Y.F. Rao, W. Chu, Y.R. Wang, Appl. Catal. A Gen. 468 (2013) 240–249.
[55] Z. Zhu, Y. Chen, Y. Gu, F. Wu, W. Yan, T. Xu, W. Chen, Water Res. 93 (2016) 296–305.